Simplified model of a dual-media molten-salt thermocline tank with a multiple layer wall

M. Fernández-Torrijos[a,], C. Sobrino[a], J. A. Almendros-Ibáñez[b,c]

[a]*Universidad Carlos III de Madrid, ISE Research Group, Thermal and Fluid Engineering Department, Avda. de la Universidad 30, 28911 Leganés, Madrid, Spain*
[b]*Escuela de Ingenieros Industriales, Dpto. de Mecánica Aplicada e Ingeniería de Proyectos, Castilla La Mancha University, Campus universitario s/n, 02071, Albacete, Spain*
[c]*Renewable Energy Research Institute, Section of Solar and Energy Efficiency, C/ de la Investigación s/n, 02071, Albacete, Spain*

Abstract

Thermal ratcheting is a critical phenomenon associated with the cyclic operation of dual-media thermocline tanks in solar energy applications. To study this phenomenon, it is necessary to develop a comprehensive model of a thermocline tank that includes both the heterogeneous filler region and the composite tank wall. Because CFD models require a high computational cost to simulate a thermocline tank considering transient state operation, a simplified dual-phase model that includes the unsteady heat transfer through a multiple layer wall has been developed. The filler region consists of a rock bed with interstitial molten salt, and the tank wall is composed of a steel shell with two layers of insulation (firebrick and ceramic). In this simplified model, the fluid flow inside the tank is considered to be one-dimensional along the tank axis direction, whereas the heat conduction in the composite wall is considered to be two-dimensional. Therefore, a convective heat transfer coefficient from the bed to the wall is necessary to couple the molten salt flow with the heat transfer in the tank shell. In this work, the effects of both convective heat transfer from the bed to the wall and molten salt flow rate on the time-dependent thermal response of both the steel shell and molten salt have been analyzed. The simplified model is able to predict the temperatures of the molten salt, filler material and layer wall as well as the

---

Email address: `ftorrijo@ing.uc3m.es` (M. Fernández-Torrijos)

mechanical stress in the tank shell.

1. Introduction

Concentrated solar power (CSP) is one of the most promising large-scale renewable energy technologies. However, CSP is subject to the inherent variations in weather conditions; thus, it requires energy storage technologies to provide steady power output (Ibrahim et al., 2008). A single dual-media thermocline tank is a low-cost alternative to conventional multiple-tank systems for concentrating solar power thermal energy storage. Typical dual-media thermocline tanks contain molten salt, which is used as the heat transfer fluid (HTF), and a filler material compatible with molten salts (i.e., quartzite rock (Pacheco et al., 2002)) that provides sensible heat capacity at a reduced cost. In a thermocline tank, both the cold and hot reserves of HTF are stored in a single tank. Stable thermal stratification of the fluid region is maintained by buoyancy forces generated by the difference in density between the hot and cold HTF. Therefore, the cold reserve of HTF is placed in the lower portion of the tank, while the hot HTF remains in the upper portion. The cold and hot regions are separated by a thin slice of the tank, which experiences a large temperature gradient known as the thermocline or heat-exchange region. The potential cost advantages of the thermocline result from the use of one tank rather than two tanks and a considerably lower volume of solar salt (Kolb, 2011). Pacheco et al. (2002) estimated that the cost of a dual-media thermocline tank storage system is approximately 2/3 the cost of a two-tank molten salt system for parabolic trough power plants. Flueckiger et al. (2014) developed a one-dimensional simplified model to simulate the behavior of an adiabatic thermocline tank, which solves the energy transport in the porous region to calculate the temperature fields of both the molten salt and filler material. The velocity field inside the porous bed was obtained by an expression that relates it with the fluid density field. This ex-

2

pression was obtained from the inherent relationship between the speed of the heat-exchange region and the velocity of the molten salt entering the filler bed previously reported by Yang and Garimella (2010b):

$$u_{in} = \frac{\varepsilon \, \rho_{f,in} \, c_{p,f} + (1 - \varepsilon) \, \rho_s \, c_{p,s}}{\rho_{f,in} \, c_{p,f}} \, v \tag{1}$$

where the subindex in refers to the axial position of the inlet of the molten salt and v is the speed of the heat-exchange region. Equation (1) was obtained via a simple energy balance on a control volume that covers the molten salt and filler in the entire heat-exchange zone and that does not include the heat looses through the tank wall. Flueckiger et al. (2014) reformulated Equation (1) for an arbitrary axial location inside the bed to yield the following expression:

$$u = \frac{\varepsilon \, \rho_{f,x} \, c_{p,f} + (1 - \varepsilon) \, \rho_s \, c_{p,s}}{\varepsilon \, \rho_{f,in} \, c_{p,f} + (1 - \varepsilon) \rho_s \, c_{p,s}} \frac{\rho_{f,in}}{\rho_{f,x}} u_{in} \tag{2}$$

where subindex x refers to an arbitrary axial location inside the bed. Equation (2) was used to determine the thermocline fluid velocity throughout the porous bed without an explicit calculation of mass or momentum conservation. However, as stated above, Equation (2) does not consider the heat losses; thus, it is valid for adiabatic tank simulations.

One of the problems associated with dual-media thermocline tanks is the thermal ratcheting caused by the cyclic charge and discharge processes. During the charge half-cycle, the steel tank shell expands and the filler particles slump to fill the extra volume in the tank. During the discharge half-cycle, the steel tank shell can not recover its original shape due to the resistance posed by the rearranged filler, which results in a gradual increase of mechanical stress in the steel tank shell through repeated operation cycles (Flueckiger et al., 2011). If the stress reaches the yield strength of the wall material, then the wall plastically deforms, which could subsequently lead to an accumulation of ratchets and the possibility of structural failure of the tank. Flueckiger et al. (2011) studied the thermal and mechanical behaviors of thermocline tanks with different wall structures under different heat transfer boundaries. These authors developed a multi-dimensional two-temperature computational fluid dynamics (CFD) model

3

to simulate mass, momentum and energy transport inside a molten salt thermocline tank, which also included the energy transport in the wall. The governing conservation equations were solved by FLUENT, a commercial CFD package. Temperature profiles along the wall material were extracted from the simulation results to obtain the maximum thermomechanical stress used for predicting thermal ratcheting via both finite-element analysis and simple analytical strain relations. The results from the previous composite wall analysis could not be validated against real data because the investigated multilayer wall was not experimentally verified. Therefore, the numerical model was validated against real data through the thermomechanical simulation of the 170 MWh_t thermocline storage tank used in conjunction with the Solar One pilot plant (Flueckiger et al., 2012). The tank was filled with Caloria HT-43 mineral oil in combination with granite rock as the solid filler and operated between 204°C and 304°C. The stresses in the tank wall were monitored using strain gages placed at various tank heights and azimuth angles. Although the strain gages experienced large uncertainty, the maximum predicted hoop stress agrees to within 6.8% of the maximum stress recorded by the most reliable strain gages. Hoffmann et al. (2016) modeled pilot and lab-scale thermocline tanks to compare the accuracy and computation speed of one-dimensional single-phase versus two-phase models and evaluated the need to include the tank wall and heat losses in the simulation. They concluded that removing the wall tank reduced the computational speed by 13 %; however, if the energy stored in the wall represented more than 5 % of the total energy storage capacity, then the wall needed to be included in the simulation to achieve accurate predictions of the heat transfer fluid along the tank height and at the outlet. Nevertheless, the results of the different models presented were compared with the experimental heat transfer fluid profile from three different tank scales, but no comparison of the wall temperature profile was performed.

In this work, a simplified dual-phase model has been developed to provide a comprehensive simulation of thermocline tank operation including the unsteady heat transfer through a multiple layer wall at low computational cost. In this

model, the fluid flow inside the tank is considered to be one-dimensional along the tank axis direction, while the heat conduction in the composite wall is considered to be two-dimensional. This simplified model solves both mass and energy transport inside the tank and energy transport in each layer of the tank wall. To couple the heat transfer in the tank shell with the molten salt flow in the tank, the correlation proposed by Yagi and Kunii (1962) for the convective heat transfer coefficient from the bed to the wall was used. The temperature profiles of the steel layer were used to obtain the mechanical stress along the height of the tank through simple analytical strain relations. The simplified model was used to investigate the influence of the molten salt flow rate and convective heat transfer coefficient from the bed to the wall in the time-dependent thermal response of both the steel shell and molten salt. First, the tank was assumed to be adiabatic; thus, the energy transport of the tank wall was not included in the model. The results obtained for the adiabatic case were validated by comparison with the experimental measurements for the 2.3 MWh molten-salt tank constructed by Sandia National Laboratories (Pacheco et al., 2002). After the adiabatic model was validated against experimental measurements, the energy transport in each layer of the tank wall was included to obtain the wall temperature profile and the mechanical stress along the steel shell. The results obtained using the non-adiabatic simplified model of a dual-media molten-salt thermocline tank presented in this work were compared with those obtained by the CFD model developed by Flueckiger et al. (2011).

2. Numerical modeling

2.1. Problem description

In this work, a continuous solid phase model has been developed in which the solid is assumed to behave as a continuous, homogeneous and isotropic medium. The fluid flow inside the tank is considered to be one-dimensional in the tank axis direction because radial temperature discrepancies are assumed to be negligible. The temperature in each solid rock is assumed to be homogeneous

5

because the Biot number of quartzite rock is approximately 0.15. Although this value exceeds the conventional limit of 0.1 for lumped capacitance, the local thermal non-equilibrium between molten salt and quartzite rock is on the order of 1 °C, and the temperature span of the thermocline is greater than 100 °C. Therefore, lumped capacitance is an acceptable assumption for the solid region (Flueckiger et al., 2014). Two alternatives for the external boundary conditions are considered on the cylindrical tank wall. The first condition assumes that the tank is adiabatic, and the second condition includes the simulation of a composite wall consisting of multiple layers. As stated in the previous section, the results obtained for the adiabatic case were validated by comparison with the measurements of the 2.3 MWh molten-salt tank constructed by Sandia National Laboratories, which was operated with a commercial molten nitrate salt mixture (60 wt% $NaNO_3$ - 40 wt% KNO_3) as the heat transfer fluid. The filler was composed of a mixture of quartzite rock and silica sand. The physical properties of the salt, which are known functions of temperature, and of the filler bed are summarized in Table 1. The bed porosity (ε) was reported to be 0.22, and the bed height (H) was reported to be 5.2 m. The tank height was 6.1 m, and the tank diameter (d_t) was 3 m. Pacheco et al. (2002) did not report the molten salt flow rate, which is needed as an input for simulating the tank. Flueckiger et al. (2014) estimated that the cold molten salt entered the packed bed at a velocity of 0.436 mm/s. The main parameters of the Sandia Laboratory experiments are summarized in Table 2, and a schematic representation of the thermocline tank is shown in Figure 1.

The numerical model of a thermocline tank that includes the filler bed and the composite wall provided in this work was validated by comparing the wall temperature profiles and the molten salt outflow temperature during the discharge process with the CFD results provided by Flueckiger et al. (2011). HITEC molten salt, which is a eutectic mixture of water-soluble inorganic salts (53 wt% KNO_3, 40 wt% $NaNO_2$, and 7 wt% $NaNO_3$), is used as the heat transfer fluid. The density, viscosity and thermal conductivity are characterized with temperature-dependent functions (Flueckiger et al., 2011), as shown in Table 1.

6

The filler material is a bed of quartzite rock with an effective diameter (d_p) of 5 cm and a bed porosity (ε) of 0.22. The properties of the solid material are summarized in Table 1. The height (H) and diameter (d_t) of the filler bed region are both fixed to 12 m. As shown in Figure 1, the tank wall is composed of multiple layers: 10 cm thick (Δfr) inner firebrick layer for thermal isolation, 2 cm thick (Δst) steel shell layer for mechanical support, and 5 cm thick (Δc) outer layer of ceramic fiber for corrosion protection and thermal isolation (Flueckiger et al., 2011). The physical properties of each layer material are summarized in Table 1. The external wall is exposed to atmosphere; thus, the thermal boundary conditions are set to a mixed convection and radiation heat transfer condition. The convection coefficient (h_∞) and the emissivity (ε_c) of the outer wall surface are fixed at 5 $W/m^2\,K$ and 1, respectively, while the ambient temperature is considered to be 27 °C. The operating temperature span of the HITEC is 293 °C to 450 °C. Although the authors did not report the molten salt flow rate, the heat-exchange region is observed to travel up the thermocline tank at a velocity of 0.4 mm/s. Thus, Equation (1) was used to calculate the hot molten salt inlet velocity $u_{in,h} = 0.33$ mm/s, as shown in Table 2, which summarizes the main parameters of the non-adiabatic thermocline tank simulated by Flueckiger et al. (2011).

[Table 1 about here.]

[Table 2 about here.]

[Figure 1 about here.]

2.2. Governing equations

2.2.1. Porous region

The mass conservation equation of the molten salt in the filler bed is stated in terms of the superficial velocity (u) as

$$\frac{\partial}{\partial t}(\varepsilon\,\rho_f) + \frac{\partial}{\partial x}(\rho_f\,u) = 0 \tag{3}$$

7

where ε is the voidage and ρ_f is the salt density.

Fluid and solid energy transport in the porous region are governed by the following conservation equations:

$$\frac{\partial}{\partial t}(\varepsilon\,\rho_f\,c_{p,f}\,T_f) + \frac{\partial}{\partial x}(\rho_f\,u\,c_{p,f}\,T_f) = \frac{\partial}{\partial x}\left(k_{f,x}\frac{\partial T_f}{\partial x}\right) + h_i\,a_p\,(T_s - T_f) + h_w\,a_w\,(T_w - T_f) \qquad (4)$$

$$\frac{\partial}{\partial t}(\rho_s\,(1-\varepsilon)\,c_{p,s}\,T_s) = \frac{\partial}{\partial x}\left(k_{s,x}\frac{\partial T_s}{\partial x}\right) - h_i\,a_p\,(T_s - T_f) \qquad (5)$$

where T_f is the molten salt temperature, T_s is the quartzite rock temperature, T_w is the wall temperature, $a_p = (6(1 - \varepsilon))/d_p$ is the superficial particle area per unit of bed volume, $a_w = 4/d_t$ is the inner wall surface area per unit of bed volume, h_i is the interstitial heat transfer coefficient, and $k_{f,x}$ and $k_{s,x}$ are the axial effective thermal conductivities of the molten salt and quartzite rock, respectively. Various correlations for the interstitial heat transfer coefficient and effective thermal conductivity were developed based on experimental results and were used in numerical models. Xu et al. (2012) investigated the general thermal behavior of a discharging process of the packed-bed thermocline system and evaluated the effects of the interstitial heat transfer coefficient, the effective thermal conductivity and the thermal conductivity of the solid fillers. They concluded that the use of different correlations for both the interstitial heat transfer coefficient and the effective thermal conductivity from the literature leads to a negligible difference in the predicted thermal performance. Increasing the coefficient from the value predicted by the correlation proposed by Wakao and Kaguei (1982) by 10 times or even 100 times could not further alter the temperature profile, whereas decreasing the interstitial heat transfer coefficient resulted in an evident expansion of the heat-exchange region. In addition, variations in the effective thermal conductivity of the fluid from 0.1 to 10 W/(m K) resulted in a negligible difference in the temperature profile. Therefore, the correlations proposed by Wakao and Kaguei (1982) for both the interstitial heat transfer coefficient and the effective thermal conductivity have been employed in this work. The axial effective thermal conductivity for the fluid can be calculated

8

as

$$
k_{f,x} = \begin{cases} 0.7\,\varepsilon\,k_f & \text{for } Re \leq 0.8 \\ 0.5\,Pr\,Re\,k_f & \text{for } Re > 0.8 \end{cases} \tag{6}
$$

where k_f is the molten salt conductivity, Re is the Reynolds number based on the superficial velocity and particle diameter, and Pr is the Prandtl number. The axial effective thermal conductivity for the solid is calculated from

$$
k_{s,x} = k_e^0 + 0.5\,Pr\,Re\,k_f - k_{f,x} \tag{7}
$$

where k_e^0 is the stagnation effective thermal conductivity calculated from (Krupiczka, 1967):

$$
\frac{k_e^0}{k_f} = \left(\frac{k_s}{k_f}\right)^m \quad \text{where } m = 0.280 - 0.757\log\varepsilon - 0.057\log\left(\frac{k_s}{k_f}\right) \tag{8}
$$

and k_s is the solid conductivity. The interstitial heat transfer coefficient can be calculated using the correlation proposed by Wakao and Kaguei (1982).

$$
Nu = 2 + 1.1\,Pr^{1/3}\,Re^{0.6} \tag{9}
$$

Equation (3) provides the velocity field inside the porous bed, whereas Equations (4) and (5) provide the temperature fields of the molten salt and the quartzite rock, respectively.

2.2.2. Heat conduction in composite wall

Heat is transported by conduction in each layer of the composite wall according to the heat diffusion equation with properties inserted appropriately for each layer

$$
\frac{\partial(\rho_w\,c_{p,w}\,T_w)}{\partial t} = \nabla \cdot (k_w \nabla T_w) \tag{10}
$$

where ρ_w is the wall density, $c_{p,w}$ is the wall specific heat, and k_w is the wall conductivity. Heat conduction in the composite wall was considered to be two-dimensional to take the temperature variations along the radius and the height of the wall into account. An explicit finite difference method was used to solve the transient heat conduction equation (Blomberg, 1996). The

9

tank wall was divided into increments in the axial direction (Δx) and radial

direction (Δr). The temperature at the midpoint of cell (i,j) is called $T_{w_{i,j}}$.

The cell is an annular ring of cylindrical shape $r_j - \Delta r/2 \leq r \leq r_j + \Delta r/2$,

$x_i - \Delta x/2 \leq x \leq x_i + \Delta x/2$, as shown in Figure 2.

[Figure 2 about here.]

The thermal coupling between the cells is described by thermal conductances.

The conductance in the x-direction between cells (i-1,j) and (i,j) is

$$K_{i-0.5,j} = \frac{2\pi r_j \Delta r}{\dfrac{0.5\,\Delta x}{k_{w_{i-1,j}}} + \dfrac{0.5\,\Delta x}{k_{w_{i,j}}}} \tag{11}$$

where $k_{w_{i,j}}$ is the thermal conductivity for cell (i,j). In the same way, the

conductance between cells (i,j) and (i+1,j) is

$$K_{i+0.5,j} = \frac{2\pi r_j \Delta r}{\dfrac{0.5\,\Delta x}{k_{w_{i,j}}} + \dfrac{0.5\,\Delta x}{k_{w_{i+1,j}}}} \tag{12}$$

Because the thermal conductivity remains constant along the axial direction

($k_{w_{i-1,j}} = k_{w_{i,j}} = k_{w_{i+1,j}}$), Equation (12) results in the following expression:

$$K_{i-0.5,j} = K_{i+0.5,j} = \frac{2\pi r_j \Delta r\, k_{w_{i,j}}}{\Delta x} \quad \text{for } i = 1\ldots N \tag{13}$$

The general expression for conductance that is valid for the inner nodes along

the radial direction between cells (i,j-1) and (i,j) is

$$K_{i,j-0.5} = \frac{\Delta x}{\dfrac{1}{2\pi k_{w_{i,j-1}}}\ln\dfrac{r_{j-0.5}}{r_{j-1}} + \dfrac{1}{2\pi k_{w_{i,j}}}\ln\dfrac{r_j}{r_{j-0.5}}} \quad \text{for } j = 2\ldots M \tag{14}$$

and that between cells (i,j) and (i,j+1) is

$$K_{i,j+0.5} = \frac{\Delta x}{\dfrac{1}{2\pi k_{w_{i,j}}}\ln\dfrac{r_{j+0.5}}{r_j} + \dfrac{1}{2\pi k_{w_{i,j+1}}}\ln\dfrac{r_{j+1}}{r_{j+0.5}}} \quad \text{for } j = 1\ldots M-1 \tag{15}$$

The inner cell along the radial direction (j=1) is in contact with the molten

salt; thus, its thermal boundary condition is set to a convection heat transfer

condition. Therefore, Equation (14) results in

$$K_{i,0.5} = \frac{\Delta x}{\dfrac{1}{2\pi r_{in} h_{w_i}} + \dfrac{1}{2\pi k_{w_{i,1}}}\ln\dfrac{r_1}{r_{in}}} \tag{16}$$

where r_{in} is the inner tank radius and h_w is the convective heat transfer from the bed to the inner surface of the wall, which was calculated using the correlation proposed by Yagi and Kunii (1962). The outer cell along the radial direction (j=M) is exposed to the atmosphere; thus, its thermal boundary condition is set to a mixed convection and radiation heat transfer condition. Equation (15) results in

$$K_{1,M+0.5} = \frac{\Delta x}{\dfrac{1}{2\pi k_{w_i,M}} \ln \dfrac{r_{out}}{r_M} + \dfrac{1}{2\pi r_{out} h_{(conv+rad)_i}}} \tag{17}$$

where r_{out} is the outer tank radius and $h_{conv+rad}$ is the mixed convective and radiative heat transfer from the outer surface of the wall to the atmosphere, and it was obtained as follows:

$$h_{conv+rad} = h_\infty + \varepsilon_c \sigma_r \left(T_w(i,M) + T_\infty\right)\left(T_w^2(i,M) + T_\infty^2\right) \tag{18}$$

where h_∞ is the convection coefficient from the outer surface of the ceramic layer to the atmosphere, σ_r is the Stefan-Boltzmann constant, ε_c is the ceramic surface emissivity, and T_∞ is the temperature of the surroundings.

Figure 2 shows the four heat flows associated with an internal cell. The heat flows through the bottom ($Q_{i-0.5,j}$) and top ($Q_{i+0.5,j}$) boundaries of a cell are defined by the following expressions

$$Q_{i-0.5,j} = K_{i-0.5,j}\left(T_{w_{i-1,j}} - T_{w_{i,j}}\right) \tag{19}$$

$$Q_{i+0.5,j} = K_{i+0.5,j}\left(T_{w_{i,j}} - T_{w_{i+1,j}}\right) \tag{20}$$

The heat flows through the inner ($Q_{i,j-0.5}$) and outer ($Q_{i,j+0.5}$) radius boundaries are expressed as follows:

$$Q_{i,j-0.5} = K_{i,j-0.5}\left(T_{w_{i,j-1}} - T_{w_{i,j}}\right) \tag{21}$$

$$Q_{i,j+0.5} = K_{i,j+0.5}\left(T_{w_{i,j}} - T_{w_{i,j+1}}\right) \tag{22}$$

The energy conservation of the wall is solved to obtain the temperature field of the wall

$$\rho_w\, c_{p,w}\, V\, \frac{\partial T_w}{\partial t} = Q_{i-0.5,j} - Q_{i+0.5,j} + Q_{i,j-0.5} - Q_{i,j+0.5} \tag{23}$$

253 where $V = 2\pi\, r_j\, \Delta r\, \Delta x$ is the cell volume. The wall properties (ρ_w, $c_{p,w}$, and

254 $k_{w_{i,j}}$) do not remain constant along the radial distance because the tank wall is

255 composed of three different layers. Therefore, Equation (23) must be solved for

256 each layer.

<i>2.2.3. Convective heat transfer from the bed to the wall</i>

258   The correlation proposed by Yagi and Kunii (1962) was used to calculate

259 the convective heat transfer from the bed to the inner surface of the wall

$$\frac{h_w\, d_p}{k_f} = \frac{h_w^0\, d_p}{k_f} + \alpha_w\, Pr\, Re \tag{24}$$

260 where h_w^0 is the apparent wall film coefficient with a motionless fluid. Yagi

261 and Kunii (1962) observed that a value of $\alpha_w = 0.054$ properly adjusts to their

262 experimental results in a cylindrical packed bed in the range $Re_p < 2000$. The

263 apparent wall film coefficient (h_w^0) can be obtained as follows (Yagi and Kunii,

264 1962)

$$\frac{1}{h_w^0\, d_p/k_f} = \frac{1}{k_w^0/k_f} - \frac{0.5}{k_e^0/k_f} \tag{25}$$

265 where k_w^0 and k_e^0 are the equivalent thermal conductivities in the bed with a

266 motionless fluid in the region close to the surface and far from the surface,

267 respectively. Kunii and Smith (1960) proposed a correlation to calculate the

268 equivalent thermal conductivity in the region far from the surface (k_e^0)

$$\frac{k_e^0}{k_f} = \varepsilon + \frac{\beta\,(1-\varepsilon)}{\phi + \gamma\frac{1}{\kappa}} \tag{26}$$

269 where $\beta = \Delta x_p/d_p$, $\phi = l_v/d_p$, $\gamma = l_s/d_p$, and $\kappa = k_s/k_f$. Δx_p is the effective

270 length between the center of two neighboring particles in the direction of the

271 heat flow, l_s is the effective length of the solid particles, and l_v is the effective

272 length of the fluid film near the stagnation point of two neighboring particles.

273 To estimate β, two particle arrangements should be considered: one for the most

274 open packing and one for close packing (Kunii and Smith, 1960). For the closest

275 packing ($\varepsilon \leq 0.26$), β should be 0.895, whereas for open packing ($\varepsilon \geq 0.476$),

276 β should be unity. Because the bed porosity of the thermocline filler bed is

277 $\varepsilon = 0.22$, a value of $\beta = 0.895$ is assumed. The value of γ depends upon l_s,

12

₂₇₈ which was assumed to be the length of a cylinder having the same volume as

₂₇₉ the spherical particle by Kunii and Smith (1960). However, Izquierdo-Barrientos

₂₈₀ et al. (2016) demonstrated that for thermal conductivities of the particles less

₂₈₁ than that of the fluid, the previous assumption predicted very high values of ϕ,

₂₈₂ which is not physically realistic. To obtain reasonable values of ϕ for any value

₂₈₃ of κ, it is assumed that the sum of both lengths, l_s and l_v, is equal to a particle

₂₈₄ diameter.

$$l_s + l_v = d_p \tag{27}$$

₂₈₅ and thus

$$\phi + \gamma = 1 \tag{28}$$

₂₈₆ The value of ϕ can be obtained by Equation (29) (Izquierdo-Barrientos et al.,

₂₈₇ 2016)

$$\phi = \frac{1}{2} \frac{\left(\frac{\kappa-1}{\kappa}\right) \sin^2 \theta_0}{\ln(\kappa - (\kappa - 1) \cos \theta_0) - \frac{\kappa-1}{\kappa}(1 - \cos \theta_0)} - \frac{1}{\kappa - 1} \tag{29}$$

₂₈₈ where θ_0 is the angle corresponding to boundary of the heat flow area for one

₂₈₉ contact point. This angle is related to the number of contact points between

₂₉₀ two neighboring particles n (Kunii and Smith, 1960) according to

$$\sin^2 \theta_0 = \frac{1}{n} \tag{30}$$

₂₉₁ The value of n depends on the particle arrangement: $n = 1.5$ for the most open

₂₉₂ packing, and $n = 4\sqrt{3}$ for close packing. Therefore, $n = 4\sqrt{3}$ is assumed in this

₂₉₃ model.

₂₉₄ The equivalent thermal conductivity in the region close to the surface can be

₂₉₅ calculated as follows (Yagi and Kunii, 1962)

$$\frac{k_w^0}{k_f} = 2\,\varepsilon_w + \frac{\beta_w(1 - \varepsilon_w)}{\phi_w + \gamma_w \frac{1}{\kappa}} \tag{31}$$

₂₉₆ where w indicates that all variables are evaluated in the region adjacent to the

₂₉₇ wall surface. As stated in Yagi and Kunii (1962), the region of the bed where

₂₉₈ the voidage is affected by the presence of the wall is extended to a distance $d_p/2$;

₂₉₉ thus, $\beta_w = 1/2$. A similar line of reasoning as that used for Equations (27) and

13

(28) is followed, which yields:

$$l_{s,w} + l_{v,w} = \Delta x_w = \frac{d_p}{2} \qquad (32)$$

and thus

$$\phi_w + \gamma_w = \beta_w = \frac{1}{2} \qquad (33)$$

The void fraction near the wall surface is assumed to have a mean value between the void fraction in the region far from the surface ($\varepsilon = 0.22$), and the void fraction in the wall is assumed in the model; therefore, $\varepsilon_w = 0.61$. Meanwhile, ϕ_w can be obtained by Equation (34) (Izquierdo-Barrientos et al., 2016)

$$\phi_w = \frac{1}{4} \frac{\left(\frac{\kappa-1}{\kappa}\right)}{\ln \kappa - \frac{\kappa-1}{\kappa}} - \frac{1}{2(\kappa-1)} \qquad (34)$$

2.2.4. Boundary conditions

During charging of the thermocline, hot molten salt enters the tank from the top, with a uniform inlet velocity u_h and temperature T_h. During discharging, cold molten salt enters the tank from the bottom, also with a uniform inlet velocity u_c and temperature T_c. The boundary conditions to solve the system of differential equations formed by Equations (3)- (5) and (10) are summarized in Table 3, and are represented in Figure 3. The adiabatic case does not simulate the composite wall, so the boundary conditions for the wall are not considered. Real tanks include two distributors above and below the porous filler bed, but these distributors are not included in the simplified model presented in this work. Thus, the adiabatic condition at the outflow boundary, from the bottom of the tank during charging or from the top of the tank during discharging, is not in accord with the physical circumstances. Therefore, a zero second derivative of the temperature was chosen as it does not fix the value of the temperature slope, so the slope of the temperature profile at a boundary node is the same as that of the previous node. Besides, the change of the boundary condition has been shown to have a negligible influence on the results, as the maximum relative difference between the results obtained with an adiabatic condition and a zero second derivative condition is below 1%.

14

2.2.5. Mechanical stress

The thermocline tank wall will exhibit corresponding temperature fluctuations along the height of the tank, which will cause expansions or contractions of the steel tank shell. As stated above, during the charge half-cycle, the internal volume of the tank increases and the filler particles settle lower to fill the additional volume; as the tank cools during the discharge half-cycle, however, the filler particles cannot be displaced upward due to gravity and inter-particle friction, which results in a gradual increase in circumferential mechanical stress in the steel tank shell through repeated operation cycles. If the stress reaches the yield strength of the wall material, then the wall plastically deforms, which could subsequently lead to an accumulation of ratchets and the possibility of structural failure of the tank. In the height direction, however, there are no structural restrictions; thus, the tank shell can expand or contract freely in this direction. Consequently, there is no axial mechanical stress in the tank. Therefore, thermal ratcheting can be produced only by the strain in the circumferential direction, which is composed of thermal strain (ϵ_T) and mechanical strain (ϵ_M) (Flueckiger et al., 2011).

$$\epsilon_L(x) = \epsilon_T + \epsilon_M \tag{35}$$

The thermal strain depends on the thermal expansion coefficient (α) of the wall material

$$\epsilon_T(x) = \alpha(T_w(x) - T_{w,ref}) \tag{36}$$

and the mechanical strain is determined by the modulus of elasticity (E) of the steel and the principal stresses (σ)

$$\epsilon_M(x) = \frac{1}{E}(\sigma_{11} - \nu(\sigma_{22} + \sigma_{33})) \tag{37}$$

The weight of the filler bed exerts some pressure on the tank wall, but it is small compared to the hoop stress due to the permanently expanded tank ra-

15

dius (Flueckiger et al., 2011). Therefore, the dependence of mechanical strain in Equation (37) may be simplified to only hoop stress. The maximum thermal strain is reached when the steel tank wall attains its maximum temperature in a charge half-cycle, whereas the mechanical strain equals 0 because the tank wall can freely expand as strain interaction with the firebrick and ceramic sections is considered negligible. These layers are composed of loosely connected blocks, so they are unable to provide structural support to the filler region (Flueckiger et al., 2011). As explained above, the rearranged filler does not allow contraction of the tank wall; thus, it is ratcheted at the geometry it reached at the maximum temperature, and the maximum amount of strain remains constant in the circumferential direction. When the tank is subsequently cooled, a portion of the thermal strain generated from the charge process converts into mechanical stress, reaching its maximum value when the steel layer is the coldest. Therefore, the maximum mechanical stress at a given location along the tank wall, which is governed by the maximum temperature fluctuation, can be expressed as follows (Flueckiger et al., 2011)

$$\sigma_{max}(x) = E\,\epsilon_{T,max}(x) = E\,\alpha(T_{w,max}(x) - T_{w,min}(x)) \tag{38}$$

For operational safety, this maximum mechanical stress must not exceed the steel yield strength (σ_y).

2.3. Solution procedure

The governing equations are numerically solved using a finite difference method, with a second-order central differencing scheme for the derivative terms of temperatures and a first-order upwind scheme for the first derivative terms of velocity. Transient discretization is performed using a fourth-order Runge-Kutta formulation with a time step of $\Delta t = 3s$ for both adiabatic and non-adiabatic cases. The numerical model was written in MATLAB software, and the simulations were conducted with an Intel(R)Core(TM) i7-4790 CPU 3.60 GHz computer processing unit.

16

The temperature fields of the molten salt, the quartzite rock, and the different wall layers were obtained using an explicit method; thus, in each time step n, the temperature fields were calculated from both temperature and velocity fields in the previous time step $n-1$. After the temperature fields were solved in the current time step, the velocity field was obtained from Equation (39) that is derived from Equation (3)

$$\frac{\partial u}{\partial x} = -\frac{1}{\rho_f}\left(\varepsilon \frac{\partial \rho_f}{\partial T_f}\frac{\partial T_f}{\partial t} + u \frac{\partial \rho_f}{\partial T_f}\frac{\partial T_f}{\partial x}\right) \tag{39}$$

Rearranging Equation (4) and substituting it into Equation (39) results in the following expression for the first derivative term of velocity,

$$\frac{\partial u}{\partial x} = -\frac{\partial \rho_f}{\partial T_f}\frac{1}{\rho_f^2 c_{p,f}}\left(\frac{\partial}{\partial x}\left(k_{f,x}\frac{\partial T_f}{\partial x}\right) + h_i\, a_p\,(T_s - T_f) + h_w\, a_w\,(T_w - T_f)\right) \tag{40}$$

Verification and validation of both adiabatic and non-adiabatic models were carried out in order to assess the accuracy of both computational simulations. Code verification can be defined as a set of methods developed to find coding mistakes, whereas solution verification is used to estimate the numerical accuracy of a particular calculation (Roy, 2005). Finally, validation is the process of determining the degree to which a model is an accurate representation of the real world (ASME, 2009). As stated above, the numerical model proposed in this work was validated by comparing the predicted results for a 2.3 MWh molten-salt tank constructed by Sandia National Laboratories against experimental measurements (Pacheco et al., 2002). These data represented temperature curves during 2 hours of discharge, but the authors did not report the initial temperature condition; thus, the first measured temperature profile was used as the initial temperature condition for the simulation. The tank constructed by S.N.L. was insulated with 23 cm of fiberglass insulation on the sides and with 20 cm of calcium silicate ridged block insulation on the top of the tank. In addition, seven electric mineral-insulated heat-trace cables, each rated at 4.8 kWe, were wrapped on the exterior surface of the tank to provide heat input during the initial heating process and to compensate for heat loss (Pacheco et al., 2002).

17

Therefore, a simulation considering an adiabatic wall was performed to validate the model against the experimental results. Moreover, a simulation that includes the composite wall of the tank, which stores and loses heat to the atmosphere, is validated against the results provided by Flueckiger et al. (2011), who solved the mass, momentum and energy conservation equations assuming axisymmetric behavior using the commercial computational fluid dynamics software FLUENT 12.1.4, and the molten salt and wall temperatures were compared. In the non-adiabatic tank simulation, the entire tank domain was initialized to the hot limit temperature. Then, nine full (discharge and charge) cycles of 12 h were simulated to avoid the influence of the initial condition and converge to the time-periodic solution. The convergence time was approximately 40 minutes. Verification and validation processes consists in quantifying the degree of accuracy inferred from the comparison of solution and data for a specified variable at a specified validation point. For the adiabatic model, the variable selected was the molten salt temperature along the tank height for the final part of the discharge ($t= 2$ h). For the non-adiabatic case, the steel shell temperature along the tank height for the final part of the discharge ($t=6.2$ h) was chosen as the variable for the verification and validation processes. The criterion used for assessing code verification was the order of accuracy test, which determines whether or not the discretization error is reduced at the expected rate. The formal order of accuracy is determined by the truncation error, whereas the observed order of accuracy is the accuracy that is directly computed from code output for a given simulation (Roy, 2005). The formal order of accuracy for molten salt and steel shell temperatures is supposed to be a value between 1 and 2 as the derivative terms of temperature were solved using a second-order central differencing scheme, but the derivative terms of velocity was discretized using a first-order scheme. For calculating the observed order of accuracy when the exact solution is not known, three numerical solutions on different meshes are needed. The observed order of accuracy is calculated as follows (Roy, 2005)

18

$$p = \frac{\ln\left(\frac{\|f_3 - f_2\|}{\|f_2 - f_1\|}\right)}{\ln r_m} \tag{41}$$

where f_3 is the solution on the coarse mesh, f_2 the solution on the medium mesh, f_1 the solution on the fine mesh, and r_m is the grid refinement factor, which is the ratio between the coarse and the fine element sizes. In this work, a value of 1.25 was selected as grid refinement factor for both adiabatic and non-adiabatic models. Therefore, mesh sizes of $\Delta x_3 = 0.00625\,H$, $\Delta x_2 = 0.005\,H$ and $\Delta x_1 = 0.0004\,H$ were used in order to obtain the three different numerical solutions for both models. Moreover, the non-adiabatic condition implies solving the heat diffusion equation in two dimensions along the wall, so mesh sizes of $\Delta r_3 = 0.075\,e$, $\Delta r_2 = 0.06\,e$ and $\Delta r_1 = 0.048\,e$ were used.

For the adiabatic case, the order of accuracy of the molten salt temperature along the tank height for the final part of the discharge was approximately 1.1 while, for the non-adiabatic case, the order of accuracy for the steel shell temperature along the tank height for the final part of the discharge was approximately 1.9. The values of the observed and formal order of accuracy do not differ greatly from each other, which indicates that both adiabatic and non-adiabatic codes accurately solve the mathematical model incorporated in each code. Solution verification consists in assessing the discretization errors present when partial differential equations are solved numerically. Grid Convergence Index (GCI) is a method for uniform reporting of grid refinement studies proposed by Roache (1994). The GCI provides an objective asymptotic approach to quantification of uncertainty of grid convergence, and is based upon a grid refinement error estimator derived from the theory of the generalized Richardson Extrapolation. The GCI is defined as follows

$$GCI = \frac{F_s}{r_m^p - 1}\left|\frac{f_2 - f_1}{f_1}\right| \tag{42}$$

where p is the order of accuracy, and F_s is a factor of safety that is usually set to three. Considering the adiabatic case, the GCI obtained for the salt outflow temperature during the final part of the discharge process was 0.5%. For the

19

⁴⁵⁹ non-adiabatic case, a GCI of 4.3% was obtained for the steel layer temperature
⁴⁶⁰ in the middle of the tank during the final stage of the discharge process.

3. Results and discussion

3.1. Adiabatic wall

⁴⁶³ As stated above, the adiabatic model was validated by means of the com-
⁴⁶⁴ parison between the numerical results and the experimental measurements per-
⁴⁶⁵ formed by Sandia National Laboratories (Pacheco et al., 2002), which is shown
⁴⁶⁶ in Figure 4. The maximum relative error between the results obtained by the
⁴⁶⁷ model presented in this work and the experimental measurements is approxi-
⁴⁶⁸ mately 2%.

⁴⁶⁹ [Figure 4 about here.]

3.2. Composite wall with heat losses

⁴⁷¹ The non-adiabatic simplified model of a dual-media molten salt thermocline
⁴⁷² tank was verified by comparing the results obtained in this work with those
⁴⁷³ obtained by the multidimensional CFD model developed by Flueckiger et al.
⁴⁷⁴ (2011). In the simplified model, the correlation proposed by Yagi and Kunii
⁴⁷⁵ (1962) for the convective heat transfer coefficient from the bed to the wall was
⁴⁷⁶ used, which provided a mean value along the tank axis of $\bar{h}_w = 90\,W/(m^2\,K)$
⁴⁷⁷ and a mean value of the wall Nusselt number of $\overline{Nu}_w = U\,H/\bar{k}_f = 155$.

⁴⁷⁹ Figure 5 shows the comparison between the steel layer temperature results
⁴⁸⁰ obtained using the model developed in this work and those of CFD results re-
⁴⁸¹ ported by Flueckiger et al. (2011). The difference between the results of both
⁴⁸² models is greater for the upper portion of the tank. In the CFD model, two
⁴⁸³ distributors above and below the porous filler bed were included. These dis-
⁴⁸⁴ tributor regions, which are free of quartzite rock, serve to maintain a uniform
⁴⁸⁵ flow condition at both ends of the filler bed. According to the CFD results,

20

the molten salt flow is turbulent in the distributor regions and has a complex structure relative to the laminar flow inside the filler bed (Yang and Garimella, 2010a). The maximum difference of 4% between the steel temperature results obtained by both the simplified and CFD models in the top of the tank is because the distributors are not included in the simplified model. Near the center of the tank height, the difference between the steel shell temperature results is approximately 3%.Table 4 shows the numerical values of the steel shell temperature for different stages of the charge and discharge processes.

[Figure 5 about here.]

[Table 4 about here.]

Figure 6 shows the outflow temperature during the discharge period, which is an indicator of the magnitude and quality of the energy recovered from the storage system. As shown in Figure 6, the profiles maintain a high temperature level for some initial part of the discharge process and then rapidly decrease in value when the heat-exchange zone approaches the top port of the tank. The high-temperature period of outflow is related to the discharge efficiency, which is the capability of a thermocline to provide useful energy, i.e., the energy retrieved above a certain temperature level that is capable of generating steam. As a comparison between the results obtained by both the CFD and simplified models, Figure 6 shows the average molten salt outflow temperature during the discharge process over all cases with varying surface conditions and composite wall thicknesses studied by Flueckiger et al. (2011). The variation between the cases is represented by error bars equal to two standard deviations. It is shown that the results obtained by the simplified model presented in this work using the correlation proposed by Yagi and Kunii (1962) to calculate the convective heat transfer from the bed to the wall fit reasonably well to the average molten salt outflow temperature obtained by Flueckiger et al. (2011). Table 5 shows the values of the molten salt outflow temperature for the intermediate and the final stages of the discharge process.

21

As shown in Equation (38), the maximum stress of the steel tank shell is a function of the maximum temperature fluctuation with time, which is at a maximum near the center of the tank height due to the presence of the thermocline region. The variation is minimal in the upper and lower portions of the tank because the heat-exchange region does not travel through these zones. The numerical value of the maximum stress of the steel tank shell is shown in Table 4. Figure 7 shows the comparison between the steel normalized stress with respect to the yield strength defined as

$$\omega(x) = \frac{\sigma_{max}(x)}{\sigma_y} \tag{43}$$

for both the simplified model and the CFD results of Flueckiger et al. (2011). As expected, the difference between both model stress results is larger for the upper and lower regions of the tank, where the normalized stress is minimum. However, the maximum stress along the tank wall is required to establish a design criterion for any potential tank material. The difference between the maximum stress obtained by both the simplified and CFD models is less than 1%.

A simulation using Equation (2) rather than solving the mass balance equation to calculate the velocity field was performed to compare the results obtained by both simulations. Figures 8 and 9 show the comparison between the molten salt velocity profiles for three different times during discharge and charge periods, respectively. As expected, the molten salt temperature results calculated using Equation (2) are slightly higher than those obtained by solving the mass balance equation because Equation (2) does not include heat loses through the tank wall. Therefore, the velocity results are also slightly higher, as shown in Figures 8 and 9. The maximum differences between the velocity results are observed at the beginning of the discharging process and at the end of the charging process,

22

when the influence of heat loses are higher and always close to the outlet of the mass flow: at $x = H = 12\,\mathrm{m}$ during the discharging process and at $x = 0\,\mathrm{m}$ during the charging process.

[Figure 8 about here.]

[Figure 9 about here.]

3.2.1. Influence of the convective heat transfer coefficient between the bed and the tank wall

In this section, the effect of the convective heat transfer coefficient on the molten salt and steel layer thermal behaviors was evaluated; thus, different convective heat transfer coefficients coming from products of the value from the correlation proposed by Yagi and Kunii (1962) and different scale factors (i.e., 0.5 and 2) are tested. Figure 10 shows the corresponding different time-dependent thermal responses of the steel shell for the different values of the convective heat transfer. As expected, the steel layer temperature and the thermal response dependence on time decrease as the convective heat transfer decreases. A lower convective heat transfer coefficient reduces sensitivity to the molten salt temperature fluctuations and diminishes the cyclic temperature variations along the steel layer. Therefore, a decrease in the convective heat transfer results in lower hoop stress near the center of the tank height. As shown in Figure 11 and also in Table 4, doubling or reducing by half the convective heat transfer coefficient results in an approximately 10% increase or reduction in the maximum mechanical stress, respectively.

Figure 12 shows the temperature histories under adiabatic ($h_w = 0$) and non-adiabatic tank wall conditions for the different values of the convective heat transfer coefficient from the bed to the wall tested. For the adiabatic case, the outflow temperature is maintained at a constant high level for the first four hours of the discharge process, whereas for the non-adiabatic wall, the high-temperature period of outflow is not held at a constant level due to the heat loss at the tank wall. Comparing the results obtained for the non-adiabatic

23

case, Figure 12 shows that an increase in the convective heat transfer coefficient results in a shorter high-temperature period of outflow and thus a lower thermocline efficiency.

[Figure 10 about here.]

[Figure 11 about here.]

[Figure 12 about here.]

3.2.2. Influence of molten salt flow rate

To analyze the influence of the molten salt flow rate on the time-dependent thermal response of the steel shell, different values of Re were tested in this work. The results stated in the previous section were obtained using $Re = 20$, whereas three new cases with $Re = 50$, 100, and 200 were simulated in this section, and the numerical results are shown in Tables 4 and 5. Figure 13 shows the temperature profiles along the steel shell during the discharge period for $Re = 20$ and 200 at different non-dimensional times, defined as $\tau = t\,u_{in,h}/H$. Increasing the Reynolds number results in a higher steel shell temperature because of the increase in the convective heat transfer coefficient from the bed to the wall and the decrease in the discharge time, which minimizes the influence of energy loss at the tank wall. For $Re = 200$, the steel shell temperature remains constant during the discharge process; thus, the maximum hoop stress is drastically reduced to a value of 0.01, as shown in Figure 14. Due to the thermal mass of the composite wall, there is a phase shift between the wall temperature response and the tank operation. For higher Reynolds numbers, there is not enough time for the wall to be affected by the cyclic molten salt fluctuations and, as a consequence, the normalized stress decreases when the Reynolds number increases.

Figure 15 shows the molten salt outflow temperatures during the discharge process for different values of Re. As explained above, the discharge time decreases as the molten salt flow rate increases; thus, the discharge times for $Re = 20$, 50, 100 and 200 are 6 h, 2.5 h, 1.25 h and 0.6 h, respectively. During

24

the early discharge process, a higher Reynolds number results in higher outflow temperatures due to the lower influence of energy loss at the tank wall. At the end of the discharge process, however, the outflow temperature for $Re = 200$ is slightly lower than those for $Re = 50$ and $Re = 100$. The overall energy efficiency of a thermal energy storage system is defined in this work as the ratio between the energy recovered from TES during discharging and the energy input to TES during charging (Dinçer and Rosen, 2002). Because not all the energy recovered from a thermocline is useful in generating superheated steam, the energy efficiency is calculated as follows

$$\eta = \frac{E(\Theta_H > \Theta_0)_{out,dis}}{E_{in,chg}} \tag{44}$$

where Θ_H is the non-dimensional molten salt temperature at the top port of the tank and Θ_0 is a threshold value determined by the application of interest. A value of 0.95 for Θ_0 is chosen, so thermal energy delivered at temperatures greater than 442 °C is considering useful in generating superheated steam for the steam turbine. The useful energy delivered during discharging is obtained as follows

$$E(\Theta_H > \Theta_0)_{out,dis} = \int_0^{t_{us}} \dot{m}_f \, c_{p,f} \, (T_H(t) - T_c) \, dt \tag{45}$$

where T_H is the molten salt temperature at the top port of the tank, T_c is the cold operation limit, and t_{us} is the discharge time while the temperature at the top port of the tank remains above the threshold value. The energy input to the thermocline tank during charging is calculated as

$$E_{in,chg} = \int_0^{t_{chg}} \dot{m}_f \, c_{p,f} \, (T_h - T_C(t)) \, dt \tag{46}$$

where T_C is the molten salt temperature at the bottom port of the tank, T_h is the hot operation limit, and t_{chg} is the time during which the tank is being charged. Figure 16 shows that for an insulated thermocline tank with a wall Nusselt number of approximately 10^2, the overall energy efficiency first increases and then decreases as the Reynolds number increases. The initial increase indicates that a higher discharge time and therefore higher effects of energy loss for lower

25

Re has a dominant influence on the discharge efficiency. However, at higher
Reynolds numbers, the heat-exchange region expands. Because the molten salt
in the heat-exchange region is at a relatively lower temperature, expansion can
lead to a significant waste of thermal energy (Yang and Garimella, 2010b). As
shown in Figure 16, for higher Reynolds numbers, although the effects of the heat
loss in the tank wall are minimized, the expansion of the heat-exchange zone has
a more important effect on the efficiency. The maximum overall energy efficiency
is achieved for $Re = 100$, and the maximum normalized stress is decreased from
0.42 for $Re = 20$ to 0.072 for $Re = 100$, as shown in Figure (14). Therefore,
$Re = 100$ is the optimum Reynolds number for both maximum overall energy
efficiency and lower steel shell stress for the tank simulated in this work.

[Figure 13 about here.]

[Figure 14 about here.]

[Figure 15 about here.]

[Figure 16 about here.]

4. Conclusions

A simplified dual-phase model for a molten-salt thermocline tank with a
complex wall consisting of multiple layers was developed to solve mass and en-
ergy transport with a low computational cost. The model was used to obtain
the time-dependent thermal response of the steel shell to study the potential for
failure of the tank shell wall by thermal ratcheting. Because the fluid flow inside
the tank is considered to be one-dimensional in the tank axis direction, a convec-
tive heat transfer coefficient from the bed to the wall is necessary to couple the
molten salt flow with the heat transfer in the tank shell. In this work, the influ-
ence of the convective heat transfer coefficient on the molten salt and steel layer
thermal behaviors has been analyzed. Higher heat transfer coefficients result in
higher steel layer temperatures, as well as higher stress in the tank wall, due to

26

the higher sensitivity of the wall to the molten salt temperature fluctuations. Doubling or reducing by half the convective heat transfer coefficient results in an approximately 10% increase or decrease in the maximum mechanical stress, respectively. As expected, the thermocline energy efficiency is reduced when the heat transfer coefficient increases because of the higher influence of energy loss at the tank wall. The correlation proposed by Yagi and Kunii (1962) for the bed to wall heat transfer coefficient led to the wall temperature profiles obtained using the simplified one-dimensional model exhibiting good agreement with a multi-dimensional CFD model. The maximum difference between the steel temperature results obtained by both models is 4%.

In addition, the influence of the molten salt flow rate on the time-dependent thermal response of both the steel shell and molten salt has been analyzed. Increasing the mass flow rate of the molten salt in the tank has an effect of increasing the convective heat transfer coefficient from the bed to the wall and decreasing the dimensional discharge time, resulting in a higher temperature of the steel layer. Although the steel temperature is higher, the potential for failure of the tank shell wall by thermal ratcheting is reduced because there is not enough time for the wall to be affected by the cyclic molten salt fluctuations. For the thermocline tank studied in this work, which has a wall Nusselt number of approximately 10^2, increasing the molten salt flow rate results in an initial increase of the overall energy efficiency for $Re < 100$ and a subsequent decrease of the efficiency for $Re > 100$. The initial increase indicates that the increased discharge time has a dominant influence on the discharge efficiency, whereas the subsequent decrease shows that the expansion of the heat-exchange zone caused by the increase in Reynolds number has a more important effect on the efficiency. Therefore, the maximum overall energy efficiency is reached for $Re = 100$, which corresponds to a low steel shell stress and thus a low potential for failure of the tank wall by thermal ratcheting. Therefore, for thermocline tanks with a wall Nusselt number of approximately 10^2, there is an optimum value of molten salt flow rate that maximizes the overall energy efficiency and minimizes the steel shell stress.

27

5. Notation

a_p Superficial particle area per unit of bed volume $[\mathrm{m}^{-1}]$

a_w Inner wall surface area per unit of bed volume $[\mathrm{m}^{-1}]$

c_p Specific heat $[\mathrm{J/(kg\,K)}]$

d_p Diameter of filler particle $[\mathrm{m}]$

d_t Inner diameter of the tank $[\mathrm{m}]$

e Wall thickness $[\mathrm{m}]$

E Modulus of elasticity $[\mathrm{GPa}]$

F_s Safety factor $[\text{-}]$

h Heat transfer coefficient $[\mathrm{W/(m^2\,K)}]$

h_i Interstitial heat transfer coefficient $[\mathrm{W/(m^2\,K)}]$

$h_{conv+rad}$ Mixed convective and radioactive heat transfer coefficient from the outer surface of the wall to the atmosphere $[\mathrm{W/(m^2\,K)}]$

h_w Convective heat transfer coefficient from the bed to the inner surface of the wall $[\mathrm{W/(m^2\,K)}]$

h_∞ Convective heat transfer coefficient from the outer surface of the ceramic layer to the atmosphere

28

H Filler bed height [m]

k Thermal conductivity [W/(m K)]

$k_{f,x}$ Axial effective thermal conductivity of the molten salt [W/(m K)]

$k_{s,x}$ Axial effective thermal conductivity of the filler bed [W/(m K)]

K Conductance [W/K]

l_s Effective length of the solid particles [m]

l_v Effective length of the fluid film near the stagnation point of two neighboring particles [m]

Nu_w Wall Nusselt number, $Nu_w = U\,H/\bar{k}_f$ [-]

Re Reynolds number, $Re = \frac{\rho_f\,u\,d_p}{\mu_f}$ [-]

p Order of accuracy, [-]

Pr Prandtl number, $Pr = \frac{\mu_f\,c_{p,f}}{k_f}$ [-]

Q Heat flow [W]

r Radial location [m]

r_{in} Inner tank radius [m]

r_{out} Outer tank radius [m]

r_m Grid refinement factor [-]

R Non-dimensional radial location $R = \dfrac{r}{H}$ [-]

t Time [s]

726   T Temperature [°C]

727   u Molten salt superficial velocity [m/s]

728   U Overall heat transfer coefficient [W/(m^2 K)]

729   v Speed of the heat-exchange region [m/s]

730   V Cell volume [m^3]

731   x Axial location [m]

732   X Non-dimensional axial location $X = \dfrac{x}{H}$ [-]

733   *5.1. Greek symbols*

734   α Thermal expansion coefficient [K^{-1}]

735   Δc Ceramic layer thickness [m]

736   Δfr Firebrick layer thickness [m]

737   Δst Steel layer thickness [m]

738   Δx_p Effective length between the center of two neighboring particles [m]

739   ε Porosity [-]

740   ε_c Emissivity of ceramic material [-]

741   ϵ_L Strain in circumferential direction [-]

742   ϵ_M Mechanical strain [-]

743   ϵ_T Thermal strain [-]

744 ν Poission's ratio [-]

745 Θ Non-dimensional temperature, $\Theta = \dfrac{T - T_c}{T_h - T_c}$ [-]

746 ρ Density [kg/m^3]

747 σ Stress [Pa]

748 σ_y Yield strength [MPa]

749 σ_r Stefan-Boltzmann constant, 5.67×10^{-8} [W/(m^2 K^4)]

750 τ Non-dimensional time, $\tau = \dfrac{t\,u_{in}}{H}$ [-]

751 ω Stress ratio [-]

752 *5.2. Subscripts*

753 c Cold operation limit

754 C Bottom port of the tank

755 chg Charge period

756 dis Discharge period

757 e Bed region far form the surface

758 f Liquid salt phase

759 h Hot operation limit

760 H Top port of the tank

761 i Node number along the axial direction

in Inlet to the filler region

j Node number along the radial direction

s Solid filler phase

us Useful

w Wall

1   Fine mesh

2   Medium-sized mesh

3   Coarse mesh

5.3. Superscripts

0   Motionless fluid

References

References

ASME, 2009. V&v 20-2009: Standard for verification and validation in computational fluid dynamics and heat transfer.

Blomberg, T., 1996. Heat conduction in two and three dimensions. computer modelling of building physics applications. Ph.D. thesis, Lund University.

Dinçer, I., Rosen, M. A., 2002. Thermal Energy Storage. Systems and Applications. JOHN WILEY & SONS, LTD.

Flueckiger, S., Yang, Z., Garimella, S., 2011. An integrated thermal and mechanical investigation of molten-salt thermocline energy storage. Applied Energy 88, 2098–2105.

32

Flueckiger, S., Yang, Z., Garimella, S., 2012. Thermomechanical simulation of the solar one thermocline storage tank. ASME Journal of Solar Energy Engineering 134, 041014.

Flueckiger, S. M., Iverson, B. D., Garimella, S. V., Pacheco, J. E., 2014. System-level simulation of a solar power tower plant with thermocline thermal energy storage. Applied Energy 113, 86–96.

Hoffmann, J. F., Fasquelle, T., Goetz, V., Py, X., 2016. A thermocline thermal energy storage system with filler materials for concentrated solar power plants: Experimental data and numerical model sensitivity to different experimental tank scales. Applied Thermal Engineering 100, 753–761.

Ibrahim, H., Ilinca, A., Perron, J., 2008. Energy storage systems: Characterisctis and comparisons. Renewable Sutainable Energy Rev 12, 1221–1250.

Izquierdo-Barrientos, M. A., Sobrino, C., Almendros-Ibáñez, J., 2016. Modeling the heat transfer coefficient between a surface and fixed and fluidized beds with phase change material. ASME Journal of Heat Transfer 138, 072001.

Kolb, G. J., 2011. Evaluation of annual performance of 2-tank and thermocline thermal storage systems for trough plants. ASME Journal of Solar Energy Engineering 133, 031023.

Krupiczka, R., 1967. Analysis of thermal conductivity in granular materials. International Chemical Engineering 7, 122–144.

Kunii, D., Smith, J. M., 1960. Heat transfer characteristics of porous rocks. AIChE Journal 6, 71–78.

Pacheco, J. E., Showaltera, S. K., Kolb, W. J., 2002. Development of a molten-salt thermocline thermal storage system for parabolic trough plants. Journal of Solar Energy Engineering 124, 153–159.

Roache, P. J., 1994. Perspective: A method for uniform reporting of grid refinement studies. Journal of Fluids Engineering 116, 405–413.

Roy, C. J., 2005. Review of code and solution verification procedures for computational simulation. Journal of Computational Physics 205, 131–156.

Wakao, N., Kaguei, S., 1982. Heat and mass transfer in packed beds. Gordon and Breach Science.

Xu, C., Wanga, Z., He, Y., Li, X., Bai, F., 2012. Sensitivity analysis of the numerical study on the thermal performance of a packed-bed molten salt thermocline thermal storage system. Applied Energy 92, 65–75.

Yagi, S., Kunii, D., 1962. Studies on heat transfer in packed beds. International Development in heat transfer Part IV, 750–759.

Yang, Z., Garimella, S. V., 2010a. Molten-salt thermal energy storage in themoclines under different environmental boundary conditions. Applied Energy 87, 3322–3329.

Yang, Z., Garimella, S. V., 2010b. Thermal analysis of solar thermal energy storage in a molten-salt thermocline. Solar Energy 84, 974–985.

List of Figures

36

Figure 1: Schematic illustration of the thermocline tank with a composite wall consisting of firebrick (1), steel (2), and ceramic (3).
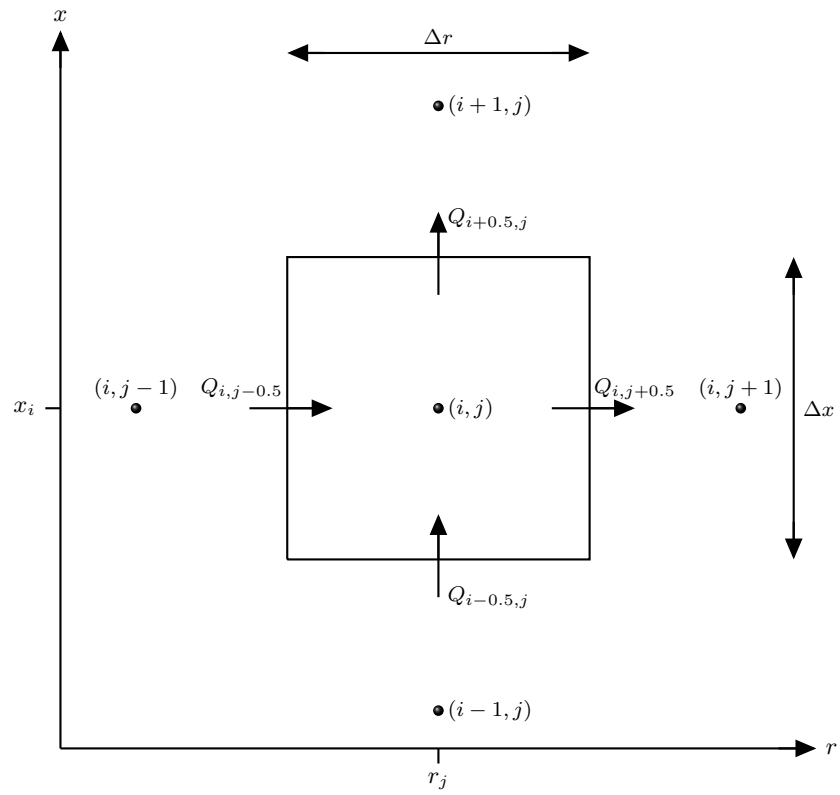
Figure 2: Mesh in cylindrical coordinates. Definitions of flows (Q) to and from cell (i,j)

$$\frac{\partial^2 Tw}{\partial x^2}=0 \quad \frac{\partial^2 Ts}{\partial x^2}=0 \quad \Big\downarrow u=u_{in,h} \ \ T=T_h \quad \frac{\partial^2 Tf}{\partial x^2}=0$$

x

r

$$\frac{\partial^2 Tw}{\partial x^2}=0 \quad \frac{\partial^2 Ts}{\partial x^2}=0 \quad \Big\uparrow u=u_{in,c} \ \ T=T_c \quad \frac{\partial^2 Tf}{\partial x^2}=0$$
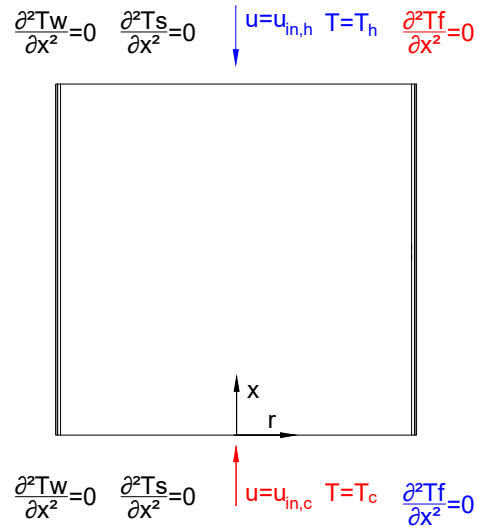
Figure 3: Boundary conditions representation for the molten salt, the filler bed and the composite wall. The boundary conditions for the molten salt during charge are presented in blue colour, while those during discharge are presented in red colour. The boundary conditions for the filler bed and the wall (only for the non-adiabatic case) remain the same during both charge and discharge processes.
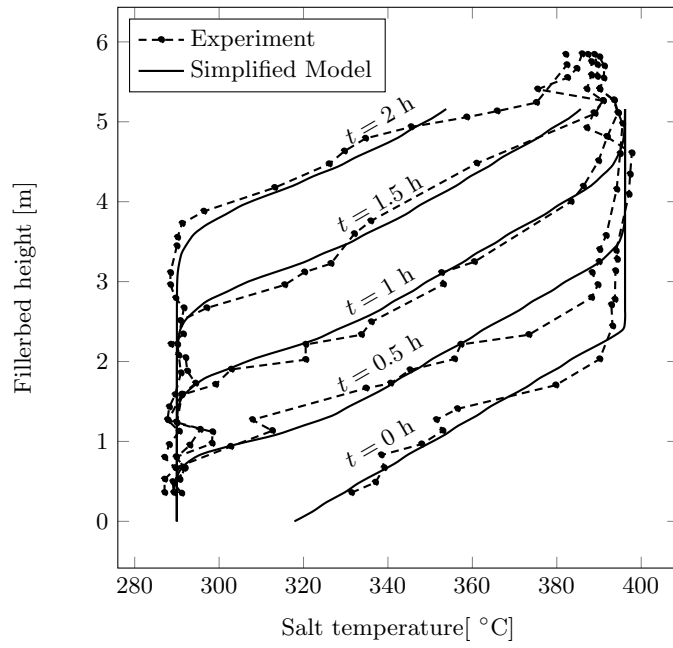
Figure 4: Comparison between the results obtained using the simplified model provided in this work and the experimental measurements performed by Sandia National Laboratories
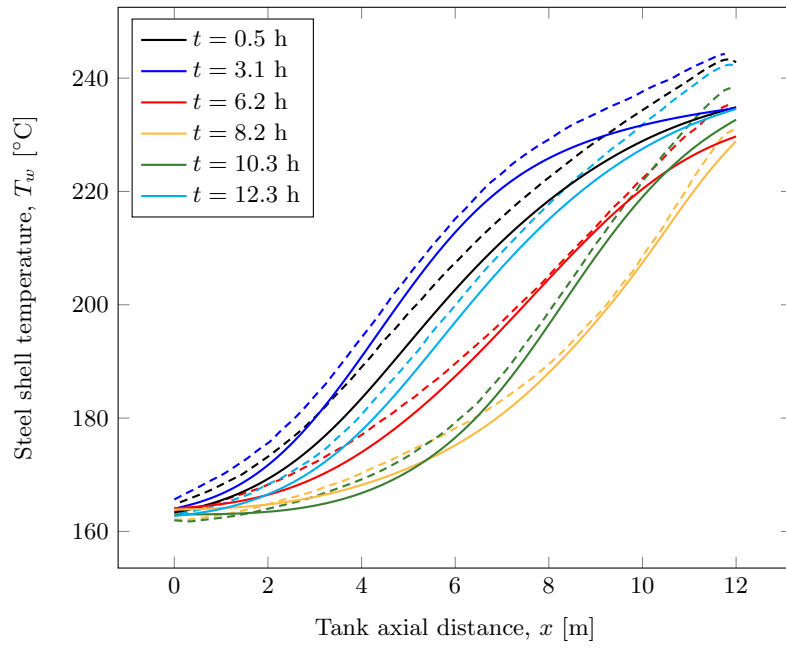
Figure 5: Temperature profiles along the steel shell. Solid lines correspond to the results obtained using the simplified model provided in this work, and dashed lines correspond to the CFD model results reported by Flueckiger et al. (2011)
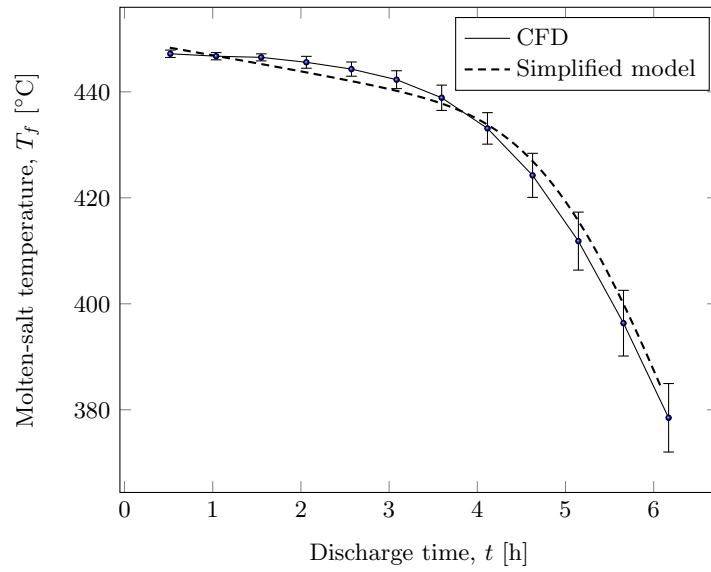
Figure 6: Molten salt outflow temperature during thermocline tank discharge. The variation between the cases studied by Flueckiger et al. (2011) is represented by error bars equal to two standard deviations.
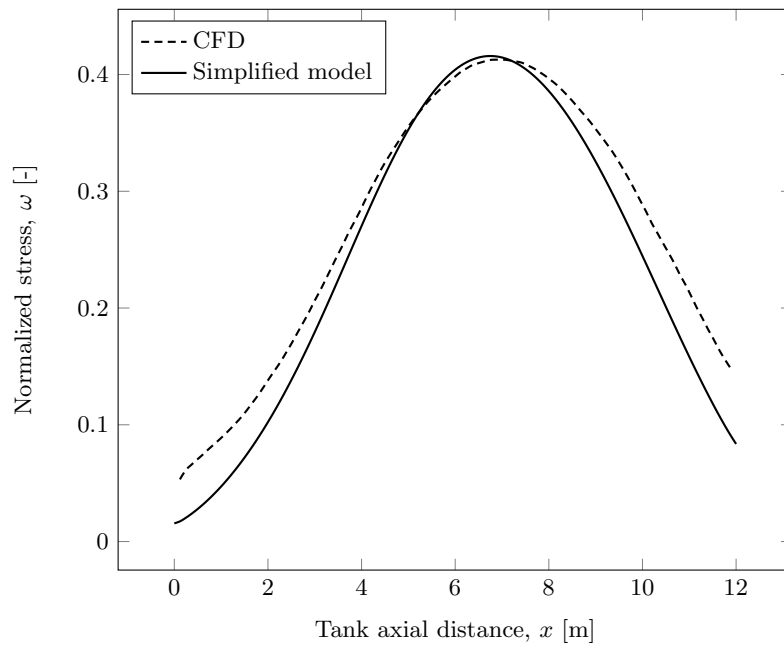
Figure 7: Hoop stress along the tank height.
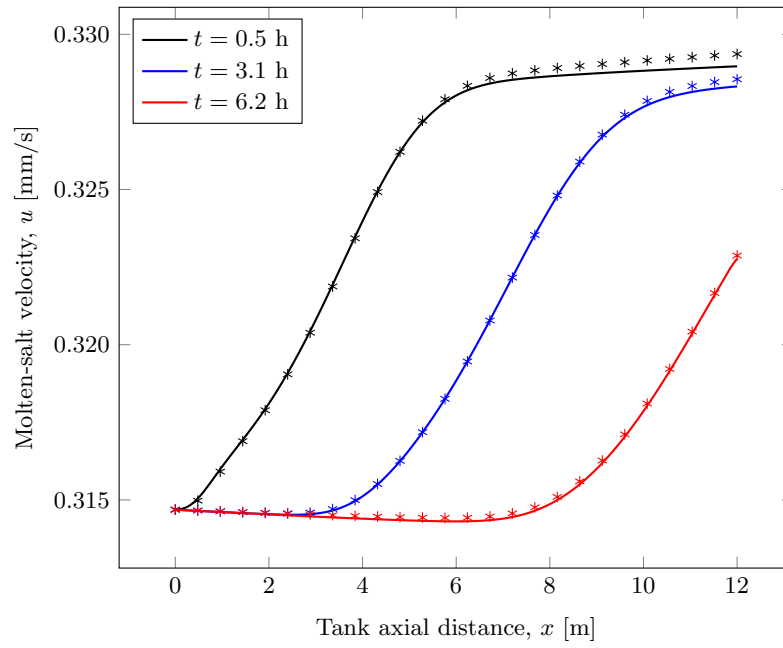
Figure 8: Molten salt velocity profiles during the discharge process. Solid lines correspond to the results obtained by solving the mass conservation equation provided, and asterisks correspond to the results obtained using Equation (2) provided by Flueckiger et al. (2014)
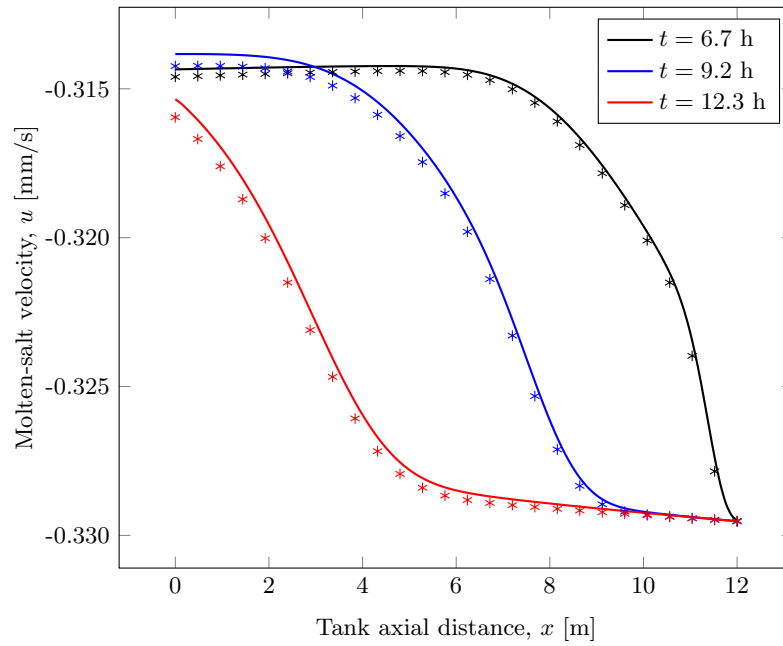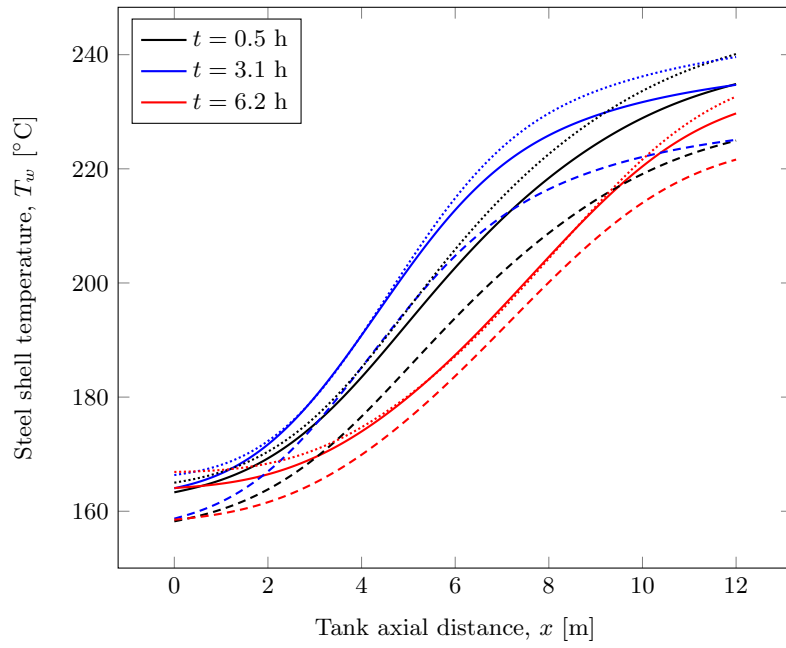
Figure 9: Molten salt velocity profiles during the charge process. Solid lines correspond to the results obtained by solving the mass conservation equation provided, and asterisks correspond to the results obtained using Equation (2) provided by Flueckiger et al. (2014)

Figure 10: Temperature profiles along the steel shell during thermocline tank discharge for different values of h_w coming from products of the value from the correlation proposed by Yagi and Kunii (1962) and different scale factors: 0.5 x h_w (dashed line), 1 x h_w (solid line), and 2 x h_w (dotted line).
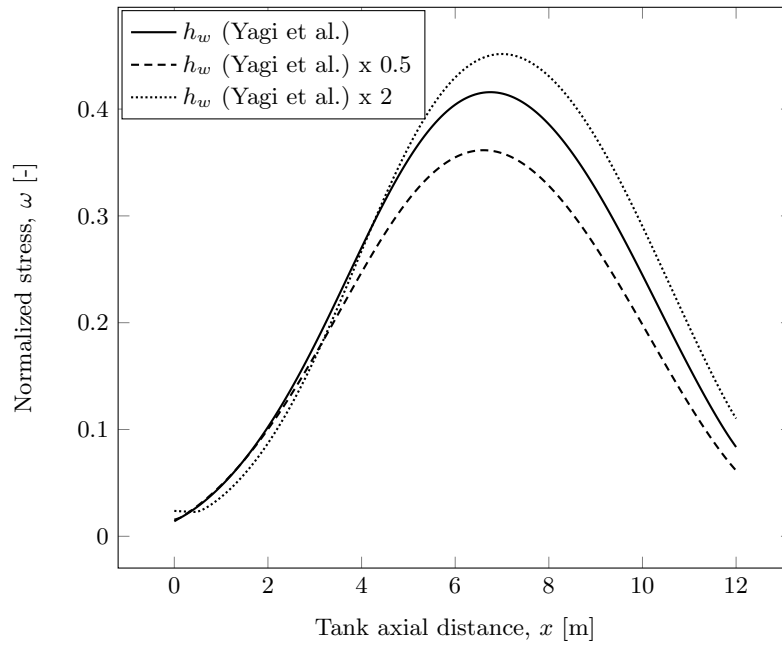
Figure 11: Hoop stress along the tank height for different values of h_w coming from products of the value from the correlation proposed by Yagi and Kunii (1962) and different scale factors: 0.5, 1, and 2.
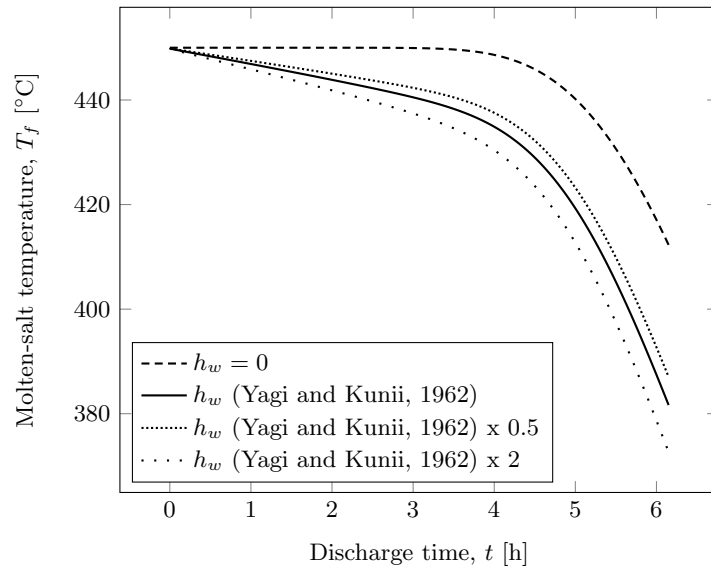
Figure 12: Molten salt outflow temperature during thermocline tank discharge for different values of h_w coming from products of the value from the correlation proposed by Yagi and Kunii (1962) and different scale factors: 0, 0.5, 1, and 2.
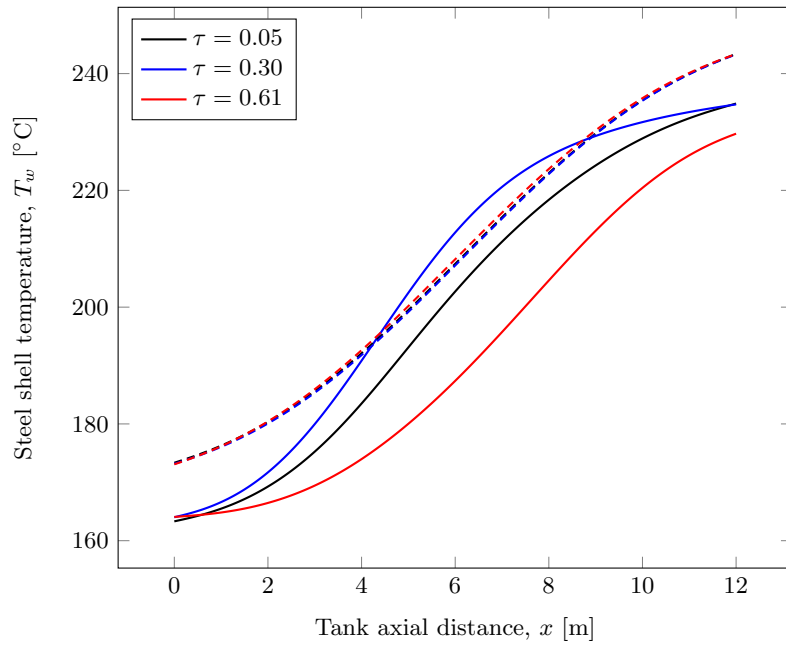
Figure 13: Temperature profiles along the steel shell during thermocline tank discharge for different values of Reynolds numbers: $Re = 20$ (solid lines) and $Re = 200$ (dashed lines).
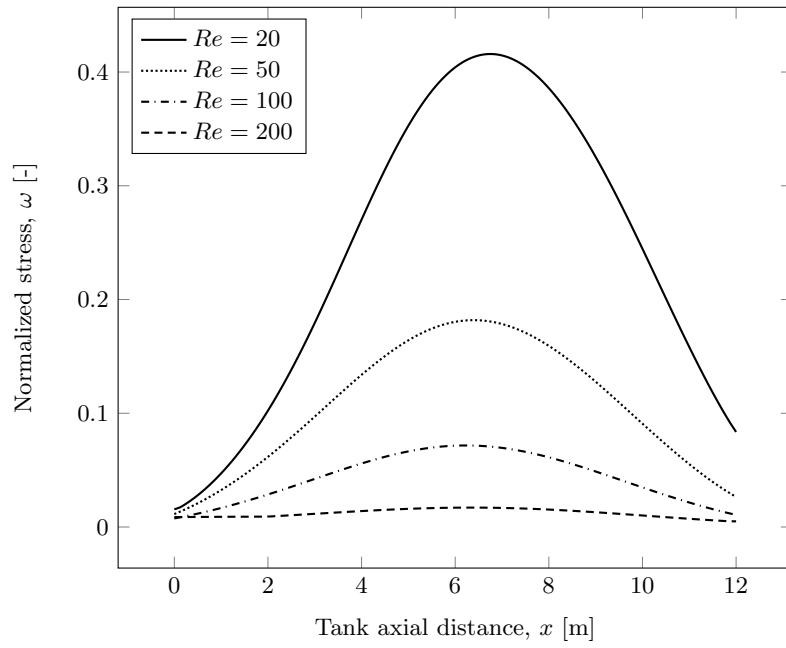
Figure 14: Hoop stress along the tank height for different values of Reynolds numbers: $Re = 20, 50, 100,$ and 200.
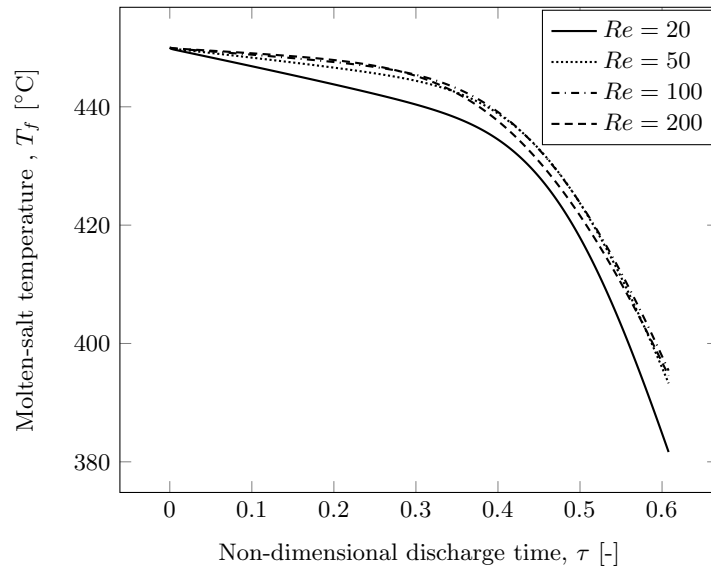
Figure 15: Molten salt outflow temperature during thermocline tank discharge for different values of Reynolds numbers: $Re = 20$, 50, 100, and 200.
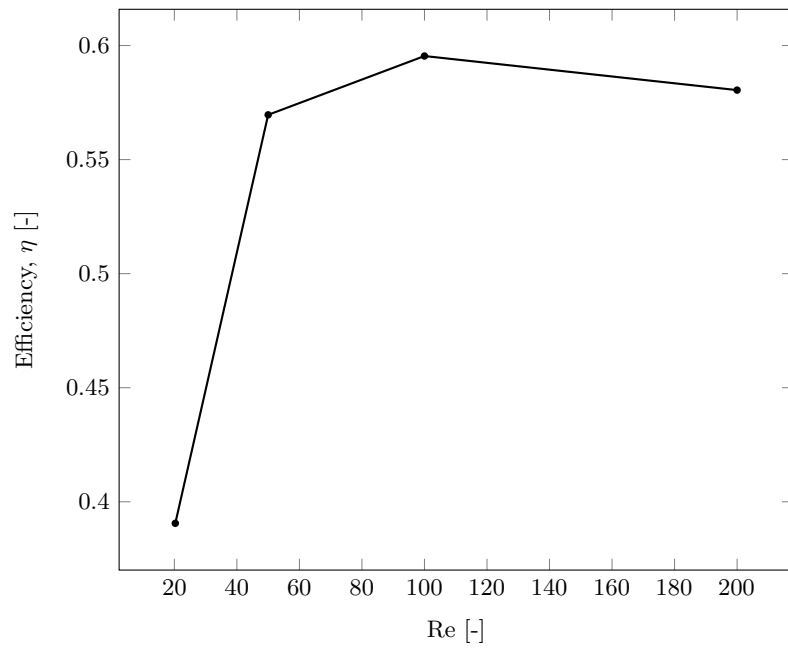
Figure 16: Discharge efficiency as a function of Reynolds number.

List of Tables

HTF	Solar Salt	ρ_l (kg/m^3)	$2090 - 0.636\,T$
		$c_{p,f}$ (J/(kg K))	1520
		k_f (J/(kg K))	$0.443 + 1.9 \cdot 10^{-4}\,T$
		μ_f (W/(m K))	$0.001(22.174 - 0.12\,T$
			$+2.281 \cdot 10^{-4}\,T^2 - 1.474 \cdot 10^{-7}\,T_l^3)$
	HITEC	ρ_l (kg/m^3)	$1838 - 0.732(T - 200)$
		$c_{p,f}$ (J/(kg K))	1561.7
		k_f (J/(kg K))	$-0.000653(T - 260) + 0.421$
		μ_f (W/(m K))	$\exp(-4.343 - 2.0143(\ln(T) - 5.011))$
TESM	Quartzite rock and silica sand	ρ_s (kg/m^3)	2500
		$c_{p,s}$ (J/(kg K))	830
		k_s ((W/(m K))	5
	Quartzite rock	ρ_s (kg/m^3)	2201
		$c_{p,s}$ (J/(kg K))	964
		k_s ((W/(m K))	5
Wall	Firebrick	ρ_{fr} (kg/m^3)	2000
		$c_{p,fr}$ (J/(kg K))	1000
		k_{fr} ((W/(m K))	1
	Steel	ρ_{st} (kg/m^3)	8000
		$c_{p,st}$ (J/(kg K))	430
		k_{st} ((W/(m K))	60
		α (K^{-1})	0.00001
		E (GPa)	200
		σ_y (MPa)	200
		ν (-)	0.3
	Ceramic	ρ_c (kg/m^3)	1000
		$c_{p,c}$ (J/(kg K))	1000
		k_c ((W/(m K))	1
		ε_c (-)	1

Table 1: Thermo-physical properties of the HTF, TESM and the different wall layers

	Sandia National Laboratory	Non-adiabatic tank CFD
HTF	Solar Salt	HITEC
TESM	Quartzite rock and silica sand	Quartzite rock
Filler bed height, H (m)	5.2	12
Tank diameter, d_t (m)	3	12
Firebrick layer thickness Δfr (m)	-	0.1
Steel layer thickness Δst (m)	-	0.02
Ceramic layer thickness Δc (m)	-	0.05
Porosity, ε (-)	0.22	0.22
Effective diameter particle, d_p (cm)	1.5	5
Cold molten salt inlet velocity, $u_{in,c}$ (mm/s)	0.436	0.315
Hot molten salt inlet velocity, $u_{in,h}$ (mm/s)	0.447	0.330
$Re = \frac{\rho_h\, u_h\, d_p}{\mu_h}$ (-)	6.8	20.3
$Pr = \frac{\mu_h\, c_{p,f}}{k_h}$ (-)	5.3	7.5
Hot operation temperature, T_h (°C)	396	450
Cold operation temperature, T_c (°C)	290	293
Discharge time, t_{dis} (h)	2	6

Table 2: Main characteristics for Sandia Laboratory experiments (Pacheco et al., 2002) and non-adiabatic CFD simulations (Flueckiger et al., 2011) used to validate the adiabatic and non-adiabatic models in this work.

	Molten salt	Quartzite rock	Wall
Charge			
$x = 0$	$\dfrac{\partial^2 T_f}{\partial x^2} = 0$	$\dfrac{\partial^2 T_s}{\partial x^2} = 0$	$\dfrac{\partial^2 T_w}{\partial x^2} = 0$
$x = H$	$T_f = T_h$ $u = u_{in,h}$	$\dfrac{\partial^2 T_s}{\partial x^2} = 0$	$\dfrac{\partial^2 T_w}{\partial x^2} = 0$
Discharge			
$x = 0$	$T_f = T_c$ $u = u_{in,c}$	$\dfrac{\partial^2 T_s}{\partial x^2} = 0$	$\dfrac{\partial^2 T_w}{\partial x^2} = 0$
$x = H$	$\dfrac{\partial^2 T_f}{\partial x^2} = 0$	$\dfrac{\partial^2 T_s}{\partial x^2} = 0$	$\dfrac{\partial^2 T_w}{\partial x^2} = 0$

Table 3: Boundary conditions for Equations (3)- (5). For the adiabatic tank, the fourth column of the table, which shows the boundary conditions of the wall, does not apply.

		Steel temperature (°C)						ω (-)
		$\tau = 0.05$	$\tau = 0.30$	$\tau = 0.61$	$\tau = 0.81$	$\tau = 1.01$	$\tau = 1.22$	
h_w (Yagi et al.)	$Re = 20$	202.67	212.79	187.38	175.21	176.56	196.94	0.42
	$Re = 50$	197.49	208.10	205.37	196.83	191.63	195.12	0.18
	$Re = 100$	201.57	205.11	207.91	205.74	202.32	200.84	0.07
	$Re = 200$	207.42	207.14	208.20	208.46	207.83	206.80	0.02
h_w x 0.5	$Re = 20$	193.86	204.75	183.69	171.63	171.91	188.87	0.36
h_w x 2	$Re = 20$	205.88	214.87	187.16	175.70	177.13	199.58	0.45

Table 4: Steel layer temperature in the medium tank height and maximum stress for different flow rates and bed-to-wall convective heat transfer coefficients. $\tau = 0.05$, 0.30 and 0.61 correspond to different stages during the discharge process, and $\tau = 0.81$, 1.01 and 1.22 correspond to different stages during the charge process.

		Outflow temperature (°C)	
		$\tau = 0.30$	$\tau = 0.61$
	$Re = 20$	440.22	381.46
h_w (Yagi et al.)	$Re = 50$	444.27	393.13
	$Re = 100$	445.28	395.41
	$Re = 200$	445.07	394.55
h_w (Yagi et al.) x 0.5	$Re = 20$	442.09	386.85
h_w (Yagi et al.) x 2	$Re = 20$	437.04	372.47

Table 5: Molten salt outflow temperature for different flow rates and bed-to-wall convective heat transfer coefficients, during discharge process: $\tau = 0.30$ corresponds to the intermediate stage, and $\tau = 0.61$ to the final stage.